



**HAL**  
open science

# Short Aromatic Diammonium Ions Modulate Distortions in 2D Lead Bromide Perovskites for Tunable White-Light Emission

Ping Fu, Michael Quintero, Claire Welton, Xiaotong Li, Bruno Cucco, Michael de Siena, Jacky Even, George Volonakis, Mikaël Kepenekian, Runze Liu, et al.

► **To cite this version:**

Ping Fu, Michael Quintero, Claire Welton, Xiaotong Li, Bruno Cucco, et al.. Short Aromatic Diammonium Ions Modulate Distortions in 2D Lead Bromide Perovskites for Tunable White-Light Emission. *Chemistry of Materials*, 2022, 34 (21), pp.9685-9698. 10.1021/acs.chemmater.2c02471 . hal-03840368

**HAL Id: hal-03840368**

**<https://hal.science/hal-03840368v1>**

Submitted on 5 Nov 2022

**HAL** is a multi-disciplinary open access archive for the deposit and dissemination of scientific research documents, whether they are published or not. The documents may come from teaching and research institutions in France or abroad, or from public or private research centers.

L'archive ouverte pluridisciplinaire **HAL**, est destinée au dépôt et à la diffusion de documents scientifiques de niveau recherche, publiés ou non, émanant des établissements d'enseignement et de recherche français ou étrangers, des laboratoires publics ou privés.

# Short Aromatic Diammonium Ions Modulate Distortions in 2D Lead Bromide Perovskites for Tunable White-Light Emission

Ping Fu,<sup>1,2</sup> Michael A. Quintero,<sup>2</sup> Claire Welton,<sup>3</sup> Xiaotong Li,<sup>2</sup> Bruno Cucco,<sup>4</sup> Michael C. De Siena,<sup>2</sup> Jacky Even,<sup>5</sup> George Volonakis,<sup>4</sup> Mikael Kepenekian,<sup>4</sup> Runze Liu,<sup>6</sup> Craig C. Laing,<sup>2</sup> Vladislav Klepov,<sup>2</sup> Yukun Liu,<sup>7</sup> Vinayak P. Dravid,<sup>7</sup> G. N. Manjunatha Reddy,<sup>3</sup> Can Li,<sup>1</sup> and Mercouri G. Kanatzidis<sup>2,\*</sup>

<sup>1</sup>State Key Laboratory of Catalysis, Dalian Institute of Chemical Physics, Chinese Academy of Sciences, Dalian National Laboratory for Clean Energy, 457 Zhongshan Road, Dalian 116023, China

<sup>2</sup>Department of Chemistry, Northwestern University, Evanston, Illinois 60208, USA.

<sup>3</sup>University of Lille, CNRS, Centrale Lille Institute, Univ. Artois, UMR 8181–UCCS– Unité de Catalyse et Chimie du Solide, F-59000, Lille, France.

<sup>4</sup>Univ Rennes, ENSCR, INSA Rennes, CNRS, ISCR (Institute des Sciences Chimiques de Rennes), UMR 6226, France

<sup>5</sup>Univ Rennes, INSA Rennes, CNRS, Institute FOTON - UMR 6082, Rennes, France

<sup>6</sup>State Key Laboratory of Molecular Reaction Dynamics and Dynamics Research Center for Energy and Environmental Materials, Dalian Institute of Chemical Physics, Chinese Academy of Sciences, Dalian 116023, China

<sup>7</sup>Department of Materials Science and Engineering, Northwestern University, Evanston, Illinois 60208, USA

White-light broadband emission in the visible range from the low-dimensional halide perovskites is commonly attributed to structural distortions in lead bromide octahedra. In this paper, we report Dion–Jacobson-phase two-dimensional (2D) lead bromide perovskites based on short aromatic diammonium cations, p-phenylene diammonium (pPDA), m-phenylene diammonium (mPDA), and two 1D compounds templated by o-phenylene diammonium (oPDA). All of the compounds exhibit white-light emission. Single-crystal X-ray diffraction analysis reveals that the distortion of the Pb octahedra is influenced by the stereochemistry of the cations and their interactions with the perovskite layers. Solid state <sup>1</sup>H and <sup>207</sup>Pb NMR spectroscopy analysis further confirms this trend, whereby different <sup>1</sup>H and <sup>207</sup>Pb chemical shifts are observed for the pPDA and mPDA spacer cations, indicating different hydrogen-bonding interactions and octahedral distortions. Owing to the octahedral distortion, 2D (mPDA)PbBr<sub>4</sub> compounds exhibit broader white-light emission than 2D (pPDA)PbBr<sub>4</sub>. Density functional theory calculations suggest that (pPDA)PbBr<sub>4</sub> and (mPDA)PbBr<sub>4</sub> are direct-band-gap semiconductors, and they exhibit larger electronic band gaps and effective masses than the Ruddlesden–Popper-phase (BA)<sub>2</sub>PbBr<sub>4</sub>. Among the films of these compounds, 2D (mPDA)PbBr<sub>4</sub> shows the best stability, which is attributed to stronger hydrogen-bonding interactions in the material.

## 1. Introduction

Organic-inorganic hybrid perovskites are promising candidates for optoelectronic devices, such as solar cells<sup>1-4</sup> and light-emitting diodes (LEDs),<sup>5,6</sup> owing to their unique optical properties and high tunability. The prototypical organic-inorganic hybrid perovskites exhibit the general formula  $AMX_3$  (A= methylammonium (MA,  $CH_3NH_3^+$ ), formamidinium (FA,  $CH_3(NH_2)_2^+$ ), or  $Cs^+$ ; M =  $Sn^{2+}$  or  $Pb^{2+}$ ; X =  $Cl^-$ ,  $Br^-$ , or  $I^-$ ). Inorganic ions form a framework with corner-sharing octahedral  $[MX_6]^{4-}$  units, and the small A-site cations occupy cuboctahedral voids within the framework and counterbalance the charge of the  $[MX_6]^{4-}$  extended anion.<sup>7</sup> When larger spacer cations are incorporated, the structure tends to split along different crystallographic planes, typically (100), (110), and (111) planes. The resulting two-dimensional (2D) perovskites have different band structures compared to their 3D counterparts and exhibit larger structural distortions within their metal halide octahedra.<sup>8-10</sup> Among them, Dion-Jacobson (DJ)-phase 2D perovskites, consisting of short diamine spacer cations between the perovskite halide slabs, represent a special class in which the slabs can come very close together and form non-bonding  $X\cdots X$  contacts.<sup>11,12</sup> This gives rise to unique phenomena, such as enhancing the electronic coupling between perovskite layers across the organic spacer and enhancing the charge transport.<sup>13</sup> Further slicing of 2D perovskites results in metal halide wires and the formation of individual octahedra, 1D and 0D structures.<sup>14</sup>

Since 2D lead bromide perovskites exhibit broadband white-light emission,<sup>15</sup> several other 2D perovskites<sup>16-18</sup> and even some lower-dimensional metal halide hybrids, such as 1D<sup>19-21</sup> and 0D perovskitoids<sup>22,23</sup> have also demonstrated white-light emission at room temperature. Because different spacer cations can impose various structural distortions, it is essential to study their effects on the nature of light emission properties of these materials. Moreover, identifying novel spacer cations will help further elucidate the relationship between cation choice, structural distortions, and light emission. Compared to the flexible aliphatic alkylammonium cations, mainly used for broad white-light emission,<sup>24-26</sup> the rigid aromatic cations offer several unique attributes to 2D perovskites. These include greater delocalization of the positive charge on the aromatic ring, shorter interlayer spacing, more hydrogen bonding between cations and anions, higher dielectric constants, and lower exciton binding energies.<sup>27,28</sup> Therefore, incorporating rigid aromatic cations into perovskite structures can result in various distortions and expansion for different types of broad-emission activity.

In this study, we employed three rigid isomers, viz. aromatic para-phenylene diammonium (pPDA), meta-phenylene diammonium (mPDA), and ortho-phenylene diammonium (oPDA) di-cations to template 2D lead bromide perovskites. We observed a nontrivial influence of each isomer on the crystal structure and physical properties. The first two cations are stabilized within the 2D perovskite motif, whereas oPDA leads to new 1D structural arrangements. The detailed crystallographic structures of 2D (pPDA) $PbBr_4$ , 2D (mPDA) $PbBr_4$ , 1D (oPDA) $_4(PbBr_4)_2Pb_3Br_{10}\cdot 4H_3PO_2$ , and 1D (oPDA) $_2Pb_3Br_{10}$  perovskites reveal the precise cation-anion interactions in these emissive materials. In addition, the local structures and packing interactions at the organic-inorganic interfaces were analyzed using  $^1H$  and  $^{207}Pb$  solid-state NMR spectra.

All the compounds exhibit white-light emission, the wavelength and width of which are linked to the level of distortion in the inorganic framework. Density functional theory calculations suggest that (pPDA)PbBr<sub>4</sub> and (mPDA)PbBr<sub>4</sub> are direct-band-gap semiconductors, and they exhibit larger electronic band-gaps and effective masses than those of the corresponding Ruddlesden-Popper phases (BA)<sub>2</sub>PbBr<sub>4</sub> (BA=butylammonium). Films of these materials were prepared successfully from N, N-dimethylformamide (DMF) solvent. The film stability test shows that the stronger hydrogen-bonding interactions in the (mPDA)PbBr<sub>4</sub> contribute to better thermal and light stability.

## 2. Results and discussion

### 2.1. Single-Crystal Growth and Structures

The new compounds were synthesized in hydrobromic acid (HBr) and hypophosphorous acid (H<sub>3</sub>PO<sub>2</sub>) medium using a step-cooling method as previously reported.<sup>29</sup> By tuning the stoichiometric ratios of lead oxide and spacer cations according to the chemical formula of (xPDA)PbBr<sub>4</sub>, 2D (pPDA)PbBr<sub>4</sub> and (mPDA)PbBr<sub>4</sub> perovskite structures are obtained in a targeted manner. The detailed procedure for the single-crystal growth is described in the experimental section. It is worth noting that the pPDA cation behaves differently in bromide and iodide chemistry. Previous work demonstrates that in the case of iodide, the pPDA cation forms a hydrated 1D perovskite structure (pPDA)PbI<sub>4</sub>•2H<sub>2</sub>O.<sup>30</sup> In the present case of bromides, we have the first example of 2D pPDAPbBr<sub>4</sub> perovskite structure (n=1) with this cation.

The oPDA cation also behaves differently in the bromide system, which does not provide any evidence for the presence of perovskite “2D (oPDA)PbBr<sub>4</sub>”. The oPDA cations give the 1D (oPDA)<sub>4</sub>(PbBr<sub>4</sub>)<sub>2</sub>Pb<sub>3</sub>Br<sub>10</sub>•4H<sub>3</sub>PO<sub>2</sub> halide when H<sub>3</sub>PO<sub>2</sub> is added to the reaction, and the 1D (oPDA)<sub>2</sub>Pb<sub>3</sub>Br<sub>10</sub> structure when the reaction is carried out without H<sub>3</sub>PO<sub>2</sub>. The morphology and color of 2D (pPDA)PbBr<sub>4</sub>, 2D (mPDA)PbBr<sub>4</sub>, 1D (oPDA)<sub>4</sub>(PbBr<sub>4</sub>)<sub>2</sub>Pb<sub>3</sub>Br<sub>10</sub>•4H<sub>3</sub>PO<sub>2</sub>, and 1D (oPDA)<sub>2</sub>Pb<sub>3</sub>Br<sub>10</sub> are shown in **Figure 1a-d**. The successful synthesis of the desired materials in their pure form is further confirmed by powder X-ray diffraction (XRD) analysis, as shown in **Figure S1**. The observed patterns match the calculated values well.

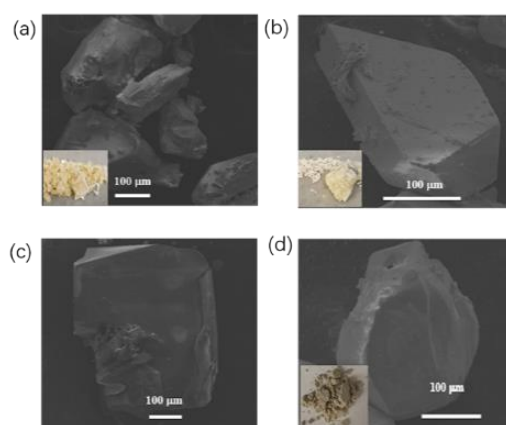


**Figure 1** | SEM images for the (a) (pPDA)PbBr<sub>4</sub>, (b) (mPDA)PbBr<sub>4</sub>, (c) (oPDA)<sub>4</sub>(PbBr<sub>4</sub>)<sub>2</sub>Pb<sub>3</sub>Br<sub>10</sub>•4 H<sub>3</sub>PO<sub>2</sub>, (d) (oPDA)<sub>2</sub>Pb<sub>3</sub>Br<sub>10</sub>, respectively. Scale bar is 100 μm.

The precise crystal structures are determined using single-crystal XRD, and they are shown in **Figure 2a-h**. The selected crystallographic data and structural refinements are listed in **Table 1**. The compounds are refined in the centrosymmetric triclinic space group ( $P\bar{1}$ ) for 2D (pPDA)PbBr<sub>4</sub> and in the monoclinic space group ( $C2/c$ ) for 2D (mPDA)PbBr<sub>4</sub>. The octahedra in (pPDA)PbBr<sub>4</sub> and (mPDA)PbBr<sub>4</sub> form “corner-sharing” 2D perovskite structures. The adjacent inorganic layer with respect to the nearest metal-metal distance for the 2D (pPDA)PbBr<sub>4</sub> and (mPDA)PbBr<sub>4</sub> are slightly offset, with a layer shift factor of (0.15, 0.15) and (0.04, 0.04), respectively, and they formally belong to the Dion-Jacobson (DJ) family ( $n=1$  members).<sup>11,31-33</sup> The adjacent [PbBr<sub>4</sub>]<sup>2-</sup> slabs are close but do not interact. For comparison, the standard van der Waals distance between the two bromine atoms is 3.7 Å. Specifically, the closest interlayer Br⋯Br distances are nonbonding at 4.43 Å and 4.60 Å for 2D (pPDA)PbBr<sub>4</sub> and 2D (mPDA)PbBr<sub>4</sub>, respectively.

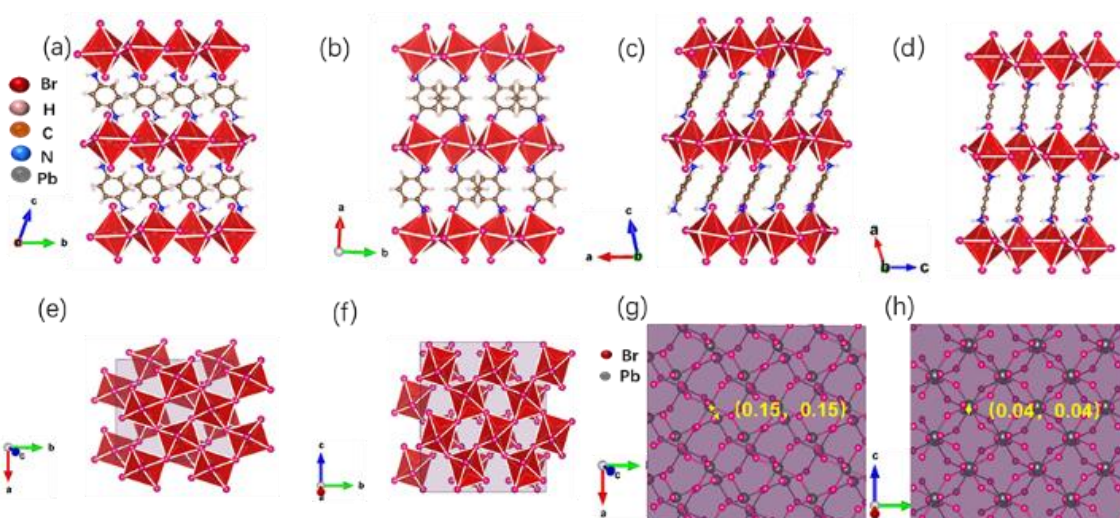


**Figure 2** | Different views of the 2D structures (a, c, e, g) (pPDA)PbBr<sub>4</sub> and (b, d, f, h) (mPDA)PbBr<sub>4</sub>, respectively. The offset of the adjacent inorganic layer is estimated by the shift distance of  $Pb/2 \times \text{length}(Pb-Br)$ .

In the ideal tetragonal structure of the  $n=1$  members, the four nearest metal atoms in a plane form a square, and the octahedra are untitled (e.g., the Pb-Br-Pb angle is 180°), but for the tilted structures, as in the present cases, two opposite edges of the square are “pulled-in” and the other two are “pushed-out.” Specifically, the average Pb-Br-Pb angles were 142.08° and 143.03° for the 2D (pPDA)PbBr<sub>4</sub> and (mPDA)PbBr<sub>4</sub>, respectively, revealing considerable octahedra tilting. For comparison, i) the typical RP phase (BA)<sub>2</sub>PbBr<sub>4</sub> and (PEA)<sub>2</sub>PbBr<sub>4</sub> (PEA: phenylethylamine), the average Pb-Br-Pb angles are 154.82° and 151.46°, respectively;<sup>34,35</sup> ii) the new hybrid layered A<sub>2</sub>PbBr<sub>4</sub> (A = 1,2,4-triazolium or acetamidinium) and AA’PbBr<sub>4</sub> (A = 1,2,4-triazolium and A’= imidazolium), templated by small disc-shaped amines, the average Pb-Br-Pb angles are 166.09°, 164.4° and 176.98°, respectively.<sup>18</sup> It is evident that the average Pb-Br-Pb angles of the 2D (pPDA)PbBr<sub>4</sub> and (mPDA)PbBr<sub>4</sub> are the smallest. Thus, the short aromatic diammonium ions can modulate much more distorted octahedra in 2D lead bromide perovskites than in the RP and hybrid layered cases. The selected bond lengths and angles in the [PbBr<sub>4</sub>] parts are listed in **Table 2**. The details of the structural distortion will be discussed later.

**Table 1 |** Crystal and Refinement Data for 2D (pPDA)PbBr<sub>4</sub>, 2D (mPDA)PbBr<sub>4</sub>, 1D (oPDA)<sub>4</sub>(PbBr<sub>4</sub>)<sub>2</sub>Pb<sub>3</sub>Br<sub>10</sub>•4 H<sub>3</sub>PO<sub>2</sub> and 1D (oPDA)<sub>2</sub>Pb<sub>3</sub>Br<sub>10</sub> at 293 K, respectively.

Empirical formula	(pPDA)PbBr <sub>4</sub>	(mPDA)PbBr <sub>4</sub>	(oPDA) <sub>4</sub> (PbBr <sub>4</sub> ) <sub>2</sub> Pb <sub>3</sub> Br <sub>10</sub> •4H <sub>3</sub> PO <sub>2</sub>	(oPDA) <sub>2</sub> Pb <sub>3</sub> Br <sub>10</sub>
Formula weight	636.99	636.99	3237.2	1640.99
Crystal system	triclinic	monoclinic	triclinic	triclinic
Space group	$P\bar{1}$	$C2/c$	$P\bar{1}$	$P\bar{1}$
Unit cell dimensions	a = 7.4473(15) Å, α = 70.53(3)° b = 8.7255(17) Å, β = 78.47(3)° c = 11.036(2) Å, γ = 89.40(3)°	a = 21.776(4) Å, α = 90° b = 8.8113(18) Å, β = 107.16(3)° c = 7.3950(15) Å, γ = 90°	a = 7.7604(16) Å, α = 89.87(3)° b = 14.578(3) Å, β = 77.79(3)° c = 16.021(3) Å, γ = 84.54(3)°	a = 7.5730(15) Å, α = 104.45(3)° b = 10.323(2) Å, β = 96.43(3)° c = 11.235(2) Å, γ = 110.67(3)°
Volume	661.2(3) Å <sup>3</sup>	1355.7(5) Å <sup>3</sup>	1763.1(7) Å <sup>3</sup>	776.2(3) Å <sup>3</sup>
Z	2	4	1	1
Density (calculated)	3.199 g/cm <sup>3</sup>	3.121 g/cm <sup>3</sup>	2.983 g/cm <sup>3</sup>	3.511 g/cm <sup>3</sup>
Index ranges	-9<h<=9, -11<=k<=10, -14<=l<=14	-28<=h<=27, -11<=k<=11, -9<=l<=9	-9<=h<=7, -17<=k<=17, -19<=l<=19	-9<=h<=12, -16<=k<=16, -17<=l<=18
Reflections collected	10586	5664	14009	12512
Independent reflections	3027 [R <sub>int</sub> = 0.0864]	1556[R <sub>int</sub> = 0.1141]	6180 [R <sub>int</sub> = 0.0529]	6702[R <sub>int</sub> =0.0471]
Completeness to θ = 25.000°	99.7%	99.5%	99.4%	99.2%
Data / restraints / parameters	3027 / 0 / 124	1556 / 0 / 65	6180 / 0 / 313	6702 / 0 / 135
Goodness-of-fit	1.172	1.122	1.024	1.035
Final R indices [I > 2σ(I)]	R <sub>obs</sub> = 0.0826, wR <sub>obs</sub> = 0.2092	R <sub>obs</sub> = 0.0507, wR <sub>obs</sub> = 0.1258	R <sub>obs</sub> = 0.0525, wR <sub>obs</sub> = 0.1357	R <sub>obs</sub> = 0.0499, wR <sub>obs</sub> = 0.1002
R indices [all data]	R <sub>all</sub> = 0.1094, wR <sub>all</sub> = 0.2600	R <sub>all</sub> = 0.0572, wR <sub>all</sub> = 0.1322	R <sub>all</sub> = 0.0652, wR <sub>all</sub> = 0.1454	R <sub>all</sub> = 0.1150, wR <sub>all</sub> = 0.1364
Largest diff. peak and hole	4.775 and -4.662 e·Å <sup>-3</sup>	2.669 and -2.365 e·Å <sup>-3</sup>	1.963 and -2.542 e·Å <sup>-3</sup>	2.048 and -3.547 e·Å <sup>-3</sup>

**Table 2 |** Bond length distortion, bond angle variance, optical band-gaps evaluated from the onset of the absorption spectra, energy at maximum PL, full width at half maximum of PL, and average lifetimes of the compounds calculated based on the 2D (pPDA)PbBr<sub>4</sub>, 2D (mPDA)PbBr<sub>4</sub>, and 1D (oPDA)<sub>4</sub>(PbBr<sub>4</sub>)<sub>2</sub>Pb<sub>3</sub>Br<sub>10</sub>•4H<sub>3</sub>PO<sub>2</sub>, respectively.

	(pPDA)PbBr <sub>4</sub>	(mPDA)PbBr <sub>4</sub>	(oPDA) <sub>4</sub> (PbBr <sub>4</sub> ) <sub>2</sub> Pb <sub>3</sub> Br <sub>10</sub> •4 H <sub>3</sub> PO <sub>2</sub>	(mPDA)PbI <sub>4</sub>
Pb-X-Pb minimum angle (X=Br, I) (°)	140.59(7)	143.03(4)	--	143.2(3)
Pb-X-Pb maximum angle (X=Br, I) (°)	143.56(9)	143.03(4)	--	144.4(2)
Pb-X-Pb average angles (X=Br, I) (°)	142.08(8)	143.03(4)	--	143.8(3)
Bond angle variance*	39.12	45.88	16.54	234.16
Bond length distortion*	0.008	0.010	0.026	0.005
Absorption edge (eV)	3.01	3.00	3.44	2.21
PL emission center (eV)	2.30	2.08	2.58	2.43
PL FWHM (eV)	0.69	0.73	0.62	0.21
CIE x	0.34	0.44	0.21	--
CIE y	0.44	0.46	0.29	--
CCT	5450	3000	>10000	--

\* The bond length distortion, (Δd) is defined by  $\Delta d = \left(\frac{1}{6}\right) \sum \left[\frac{|d_n - d|}{d}\right]$ , where d is the average Pb–Br bond distance and d<sub>n</sub> represent the six individual bond distances in the PbBr<sub>6</sub> octahedron.

Additionally, both cations have phenyl groups, aromatic ring stacking  $\pi$ - $\pi$  interactions can occur if the distance between aromatic rings ranges from 3.3 to 3.8 Å.<sup>36</sup> The distances between the stacked phenyl group for 2D (pPDA)PbBr<sub>4</sub> and 2D (mPDA)PbBr<sub>4</sub> are 3.81 Å and 3.63 Å, respectively. Both the cations in the 2D single-crystal structures have their benzene ring arranged in parallel (Figures 2c,d). The cations in (mPDA)PbBr<sub>4</sub> present stronger  $\pi$ - $\pi$  stacking interactions, while in (pPDA)PbBr<sub>4</sub> relatively weaker  $\pi$ - $\pi$  stacking interaction.

The oPDA cations template two kinds of “edge-sharing” 1D non-perovskite structures (both in the triclinic space group  $P\bar{1}$ ), based on lead bromide with or without H<sub>3</sub>PO<sub>2</sub> (Figure 3a-h). Notably, the 1D (oPDA)<sub>4</sub>(PbBr<sub>4</sub>)<sub>2</sub>Pb<sub>3</sub>Br<sub>10</sub>•4H<sub>3</sub>PO<sub>2</sub> single crystal with H<sub>3</sub>PO<sub>2</sub> has a large cell volume of 1763.1(7) Å<sup>3</sup> because of the inclusion of H<sub>3</sub>PO<sub>2</sub> molecules, while a smaller volume of 776.2(3) Å<sup>3</sup> (1763.1/2=881.5 Å<sup>3</sup> normalized) is observed for 1D (oPDA)<sub>2</sub>Pb<sub>3</sub>Br<sub>10</sub> without H<sub>3</sub>PO<sub>2</sub> molecules. The two 1D structures exhibit different unit cells, but both have two different types of zigzag 1D chains in their unit cell (Table 1). As shown in Figures 3d and 3h, one zigzag chain is connected by one edge-sharing octahedron and the other one is connected by two edge-sharing octahedra. These structures have rarely been found before and will be explained in detail below.

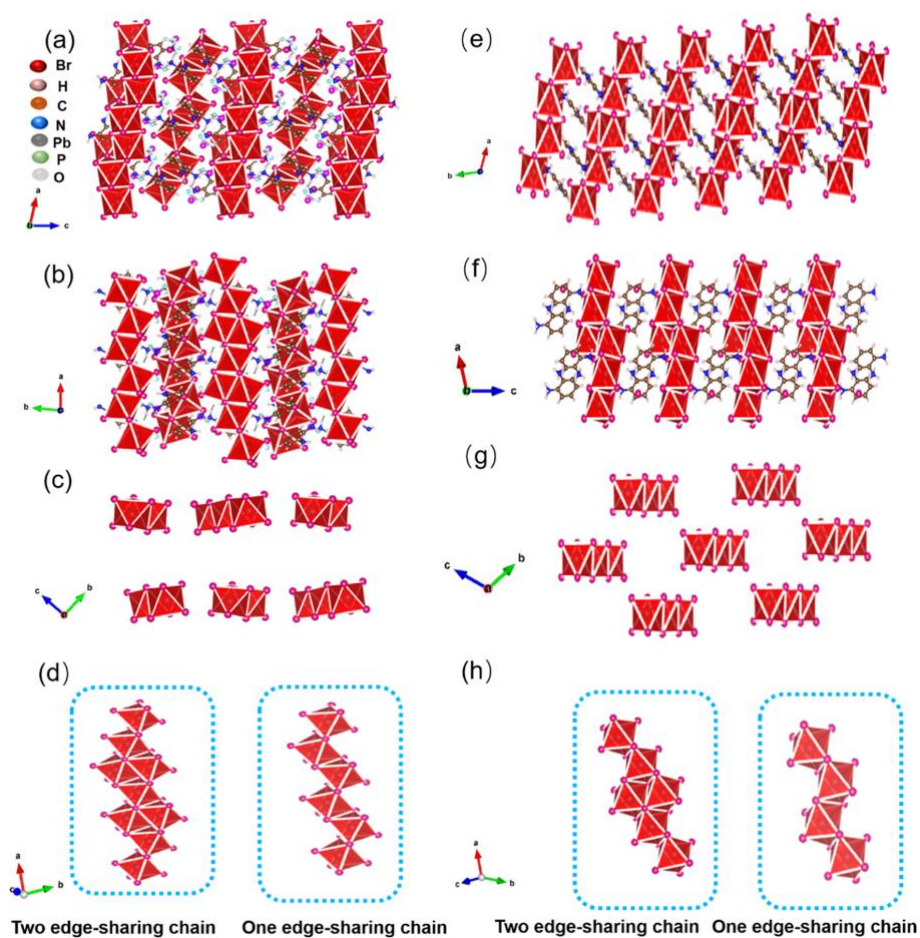


**Figure 3** | Different views of the 1D structures (a, b, c) (oPDA)<sub>4</sub>(PbBr<sub>4</sub>)<sub>2</sub>Pb<sub>3</sub>Br<sub>10</sub>•4H<sub>3</sub>PO<sub>2</sub> and (e, f, g) (oPDA)<sub>2</sub>Pb<sub>3</sub>Br<sub>10</sub>, respectively. Magnified images of one edge-sharing chain and two edge-sharing chains for (oPDA)<sub>4</sub>(PbBr<sub>4</sub>)<sub>2</sub>Pb<sub>3</sub>Br<sub>10</sub>•4H<sub>3</sub>PO<sub>2</sub> (d) and (oPDA)<sub>2</sub>Pb<sub>3</sub>Br<sub>10</sub> (h), respectively.

The short aromatic spacer cations, mPDA and pPDA strongly influence the perovskite structure and properties. To understand the distortions in these structures, we calculated the mean distortion level in the octahedra of each compound. The bond length distortion, ( $\Delta d$ ) is defined by  $\Delta d = \left(\frac{1}{6}\right) \sum \left[\frac{|d_n - d|}{d}\right]$ , where  $d$  is the average Pb–Br bond distance and  $d_n$  represent the six individual bond distances.<sup>37,38</sup> The deformation of the octahedra can also be seen from the values of the bond angle variance ( $\sigma$ ) calculated by the expression  $\sigma^2 = \sum_1^{12} i(\theta_i - 90)^2/11$ , where  $\theta_i$  is the individual Br–Pb–Br bond angle.<sup>39</sup> The bond length distortion and bond angle variance for the compounds are listed in **Table 2**. For 2D structures, the degree of bond angle variance and bond length distortion, in descending order, are 2D (mPDA)PbBr<sub>4</sub> > 2D (pPDA)PbBr<sub>4</sub>. Thus, the asymmetric arrangement of NH<sub>3</sub><sup>+</sup> groups (meta) in the aromatic diammonium ions exert larger octahedra tilting compared to the symmetric cases (para). The bond angle and bond length variance of 1D (oPDA)<sub>4</sub>(PbBr<sub>4</sub>)<sub>2</sub>Pb<sub>3</sub>Br<sub>10</sub>•4H<sub>3</sub>PO<sub>2</sub> is smaller than those of 2D compounds.

## 2.2. Cation-Anion Interactions

Hydrogen bonding plays an important role in stabilizing octahedral tilting and inducing structural distortion.<sup>40</sup> Further insights into hydrogen-bonding interactions have been drawn from the single-crystal structures. For 2D (pPDA)PbBr<sub>4</sub>, the short distances of H···Br are ~2.59, ~2.72 and ~2.88 Å, as shown in **Figure 4a**. Similarly, the distances of H···Br (~2.49 and ~2.55 Å) for 2D (mPDA)PbBr<sub>4</sub> are considerably shorter than those of 2D (pPDA)PbBr<sub>4</sub> (**Figure 4b**). Thus, the stronger hydrogen-bonding interactions in (mPDA)PbBr<sub>4</sub> might induce a larger distortion than that of (pPDA)PbBr<sub>4</sub>, which is in line with the analysis of crystal structure discussed above.

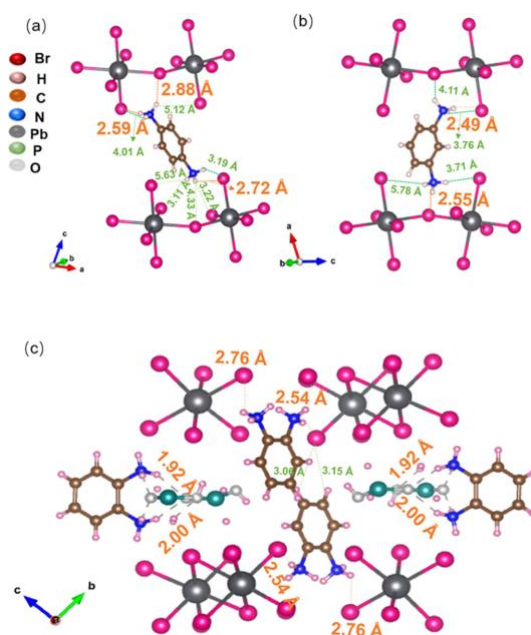


**Figure 4** | H-Br interactions for the (a) (pPDA)PbBr<sub>4</sub>, (b) (mPDA)PbBr<sub>4</sub>, (c) (oPDA)<sub>4</sub>(PbBr<sub>4</sub>)<sub>2</sub>Pb<sub>3</sub>Br<sub>10</sub>•4 H<sub>3</sub>PO<sub>2</sub>.

Considering the two 1D compounds have a similar structure, we choose 1D (oPDA)<sub>4</sub>(PbBr<sub>4</sub>)<sub>2</sub>Pb<sub>3</sub>Br<sub>10</sub>•4H<sub>3</sub>PO<sub>2</sub> for comparison in the following discussion. In 1D

(oPDA)<sub>4</sub>(PbBr<sub>4</sub>)<sub>2</sub>Pb<sub>3</sub>Br<sub>10</sub>•4H<sub>3</sub>PO<sub>2</sub> structure, the two sides of the ammonium cations can form hydrogen-bonding interactions with the molecules H<sub>3</sub>PO<sub>2</sub> as well as bromide anions (Figure 4c). Although the two sides of the ammonium cations can form hydrogen-bonding interactions with bromide anions, one H···Br bond is formed with one edge-sharing chain and the other one with two edge-sharing chains. The amino groups in the oPDA cations are tightly bound with these two kinds of chains, not with the same chain (Figure 4c). Thus, the amino groups of oPDA cations are too close to bridge with the same adjacent inorganic sheets simultaneously and unable to stabilize the 2D perovskite structures.

### 2.3. Short-Range Structures through Solid-State NMR Analysis

To further understand the organic layer and its impact on the organic-inorganic interfacial structure in these materials, we employed solid-state (ss) Nuclear Magnetic Resonance (NMR) spectroscopy. It has been used to gain insight into cation ordering and their dynamics, interfacial engineering, phase stability, and the degradation of products.<sup>41-45</sup> In this study, we used <sup>1</sup>H and <sup>207</sup>Pb magic-angle spinning (MAS) NMR spectroscopy to examine the local packing interactions of the three compounds. Particularly, <sup>1</sup>H and <sup>207</sup>Pb NMR chemical shifts are sensitive to intermolecular interactions at the organic-inorganic interface, and apical octahedral tilting.<sup>46,47</sup> For para-, meta-, and ortho-diammonium cations (Figure 5a), the different local chemical environments of the proton sites are expected to lead to different frequencies. Figure 5b compares the 1D <sup>1</sup>H NMR spectra of 2D (pPDA)PbBr<sub>4</sub>, 2D (mPDA)PbBr<sub>4</sub>, and 1D (oPDA)<sub>4</sub>(PbBr<sub>4</sub>)<sub>2</sub>Pb<sub>3</sub>Br<sub>10</sub>•4H<sub>3</sub>PO<sub>2</sub>, where the different displacements of <sup>1</sup>H chemical shifts of the -NH<sub>3</sub><sup>+</sup> groups indicate different hydrogen-bonding interactions with the PbBr<sub>6</sub> octahedra. For (pPDA)PbBr<sub>4</sub>, the partially resolved peaks at 9.2 and 8.1 ppm correspond to the -NH<sub>3</sub><sup>+</sup> (green dots) and aromatic protons (blue dots), respectively. However, the (mPDA)PbBr<sub>4</sub> phase exhibits peaks at 9.7 ppm (-NH<sub>3</sub><sup>+</sup> protons, green dots), 7.6 ppm (aromatic protons, blue dots) and a partially resolved peak at 6.8 ppm (purple dot) associated with the proton that is in the meta position with respect to -NH<sub>3</sub><sup>+</sup> groups. By analyzing and comparing the <sup>207</sup>Pb chemical shifts, we obtained insight into the organic-inorganic interfaces such as apical octahedral tilting and octahedral penetration. In the <sup>207</sup>Pb NMR spectra (Figure 5c), the pPDA and mPDA 2D phases displayed peaks at -50 and 50 ppm with a relative difference in the lead shift, Δδ = 100 ppm, corroborating the different local chemical environments of PbBr<sub>6</sub> and octahedral tilting.

For these 2D perovskites, the <sup>1</sup>H chemical shift of -NH<sub>3</sub><sup>+</sup> site at 9.7 ppm in the mPDA cation suggests stronger hydrogen-bonding interactions with lead bromide octahedra than the pPDA cations with the <sup>1</sup>H chemical shift of -NH<sub>3</sub><sup>+</sup> site at 9.2 ppm, which is in line with the analysis of crystal structure discussed above. In contrast, the 1D (oPDA)<sub>4</sub>(PbBr<sub>4</sub>)<sub>2</sub>Pb<sub>3</sub>Br<sub>10</sub>•4H<sub>3</sub>PO<sub>2</sub> displays a peak at 10 ppm associated with -NH<sub>3</sub><sup>+</sup> protons (green dots) that involve in hydrogen-bonding interactions with H<sub>3</sub>PO<sub>2</sub>. Further, a broad distribution of peaks in the 5.5-9.0 ppm range is due to aromatic protons (blue dots). As mentioned above, the -NH<sub>3</sub><sup>+</sup> groups in the oPDA cations cannot develop hydrogen-bonding interactions with the PbBr<sub>6</sub> octahedra from adjacent layers of lead octahedra owing to steric effects, thus forming a 1D phase.

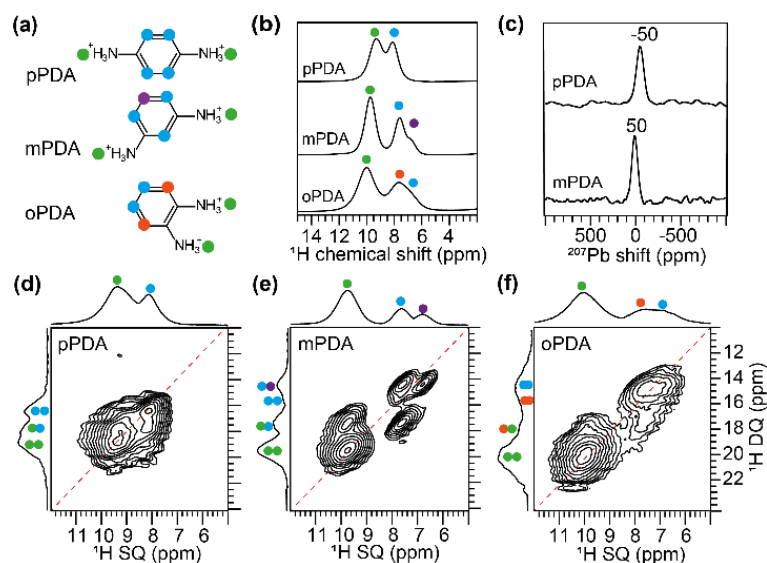


**Figure 5** | (a) Structure of p, m and oPDA spacer cations (b) solid-state 1D  $^1\text{H}$  MAS NMR spectra of (pPDA)PbBr<sub>4</sub>, (mPDA)PbBr<sub>4</sub>, (oPDA)<sub>4</sub>(PbBr<sub>4</sub>)<sub>2</sub>Pb<sub>3</sub>Br<sub>10</sub>4H<sub>3</sub>PO<sub>2</sub>, and (c) 1D  $^{207}\text{Pb}$  MAS NMR spectra of (pPDA)PbBr<sub>4</sub> and (mPDA)PbBr<sub>4</sub> perovskites. Solid-state 2D  $^1\text{H}$ - $^1\text{H}$  DQ-SQ correlation NMR spectra of (d) (pPDA)PbBr<sub>4</sub> (e) (mPDA)PbBr<sub>4</sub> and (f) (oPDA)<sub>4</sub>(PbBr<sub>4</sub>)<sub>2</sub>Pb<sub>3</sub>Br<sub>10</sub>4H<sub>3</sub>PO<sub>2</sub>, respectively. Spectral analysis is indicated by the color dots as indicated in the structures shown in (a). All spectra were acquired at 18.8 T ( $^1\text{H}$  = 800.1 MHz,  $^{207}\text{Pb}$  = 167.4 MHz), with 50 kHz MAS at room temperature.

Next, we applied 2D  $^1\text{H}$ - $^1\text{H}$  double-quantum single-quantum (DQ-SQ) correlation spectroscopy to probe packing interactions within the organic layer. In such experiments, 2D peaks are detected for through-space inter- and intramolecular dipolar-coupled  $^1\text{H}$ - $^1\text{H}$  pairs within a distance of 5 Å. These manifest as on-diagonal (chemically equivalent protons) and off-diagonal (chemically inequivalent proton sites) signals. The DQ chemical shift evolves at the sum of the SQ chemical shifts, yielding to chemical shift dispersion in the vertical DQ axis twice as large as the horizontal SQ axis. The 2D  $^1\text{H}$ - $^1\text{H}$  DQ-SQ correlation spectra of the three systems (Figures 5d–5f) show different DQ peaks, which can be attributed to different packing interactions. For 2D (pPDA)PbBr<sub>4</sub> (Figure 5d), the on-diagonal  $^1\text{H}$  DQ peak at 16.2 ppm corresponds to the intramolecular dipolar interactions between the aromatic protons as depicted by the two blue dots. The off-diagonal DQ peak at 17.5 ppm corresponds to dipolar interactions between -NH<sub>3</sub><sup>+</sup> and aromatic protons (green and blue, respectively). The on-diagonal peak at 18.8 ppm corresponds to the intramolecular dipolar interaction within the -NH<sub>3</sub><sup>+</sup> groups, as represented by the two green dots. The intermolecular contributions to this peak are negligible because the nearest distance between the intermolecular -NH<sub>3</sub><sup>+</sup> groups in pPDA cations is 5 Å. In 2D (pPDA)PbBr<sub>4</sub>, the intermolecular aromatic H-H proximities are also > 4 Å. For comparison, the  $^1\text{H}$  DQ spectrum of 2D (mPDA)PbBr<sub>4</sub> (Figure 5e) exhibits an off-diagonal DQ peak at 14.4 ppm due to the through-space inter- and intramolecular dipolar interactions between the aromatic protons as depicted in blue and purple dots, and the off-diagonal DQ peak at 17.3 ppm is due to the intramolecular through-space proximity between the -NH<sub>3</sub><sup>+</sup> (green dots) and aromatic protons (blue dots), respectively. The strong intensity on-diagonal  $^1\text{H}$  DQ peak at 19.4 ppm is due to the intramolecular dipolar

interactions in  $-\text{NH}_3^+$  groups, and the weak intensity on-diagonal  $^1\text{H}$  DQ peak at 15.2 ppm is attributable to both inter and intramolecular  $^1\text{H}$ - $^1\text{H}$  proximities between aromatic protons that are in meta position with respect to each other (blue dots) for which the interatomic distance is  $\sim 4$  Å.

For the 1D  $(\text{oPDA})_4(\text{PbBr}_4)_2\text{Pb}_3\text{Br}_{10}\cdot 4\text{PO}_2$  system (Figure 5f), we observed a broad distribution of the DQ peak at  $\sim 15$  ppm, corresponding to intra- and intermolecular interactions between the aromatic protons depicted by the two blue dots. The broad signals are due to the substantial self-assembly by oPDA cations, which lead to one-to-one as well as slip-stacked dimers, resulting in different  $\pi$ - $\pi$  stacking and C-H- $\pi$  interactions. For example, the hydrogen atoms depicted in the blue and red dots exhibit different aromatic ring current effects, leading to a broad distribution of peaks in the 6-9 ppm range. A weak off-diagonal DQ peak further corroborates this at 17.6 ppm that originates from intermolecular dipolar interactions between the aromatic (blue dots) and  $-\text{NH}_3^+$  protons (green dots) for which the intermolecular  $^1\text{H}$ - $^1\text{H}$  distance is  $\sim 3.1$  Å. In addition, the distinct on-diagonal DQ peaks at 20.2 ppm are ascribed to the intramolecular dipolar interactions between the adjacent  $-\text{NH}_3^+$  protons depicted by the two green dots. These structural differences contribute to different optical and electronic properties, as discussed below.

#### 2.4. Optical Properties, White-Light Emission and Work Functions

The optical absorption spectra of the three compounds are shown in Figure 6a. 2D  $(\text{pPDA})\text{PbBr}_4$  and  $(\text{mPDA})\text{PbBr}_4$  show sharp absorption edges and well defined excitonic peaks, respectively. Strong quantum and dielectric confinement effects owing to the organic spacers in 2D perovskites give rise to tightly bound excitons with large binding energies. Because of the excitonic peaks, it was difficult to determine the correct band-gaps for the compounds. The energies of the absorption edges are listed in Table 2. The absorption edge of 3.44 eV for 1D  $(\text{oPDA})_4(\text{PbBr}_4)_2\text{Pb}_3\text{Br}_{10}\cdot 4\text{H}_3\text{PO}_2$  is significantly larger than that of 2D perovskite compounds. This is consistent with the fact that the metal octahedra share edges in the 1D structure compared to the corner-sharing motif in perovskite structures.<sup>48,49</sup>

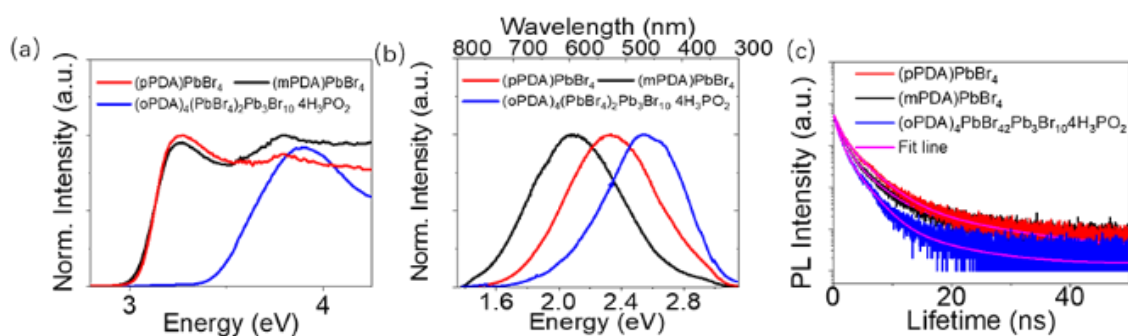


**Figure 6** | (a) Optical absorption spectra, (b) steady-state PL spectra, and (c) time-resolved PL spectra for 2D  $(\text{pPDA})\text{PbBr}_4$ , 2D  $(\text{mPDA})\text{PbBr}_4$ , 1D  $(\text{oPDA})_4(\text{PbBr}_4)_2\text{Pb}_3\text{Br}_{10}\cdot 4\text{H}_3\text{PO}_2$ , respectively.

Although the optical spectra show sharp absorption edges, the photoluminescence (PL) spectra of all the compounds exhibit broadband emission features, as shown in Figure 6b. For 2D  $(\text{mPDA})\text{PbBr}_4$ , the

maximum of PL peak is centered at 2.08 eV and the PL emission exhibits the broadest peak from 2.47 eV (502 nm) to 1.74 eV (713 nm) (Full Width Half Maximum (FWHM):0.73 eV (211 nm)) due to the largest octahedra distortion. For 2D (pPDA)PbBr<sub>4</sub>, the maximum of PL peak is centered at 2.35 eV and the PL peak exhibits the second broader peak with an FWHM of 0.69 eV (158 nm) (from 2.70 eV (459 nm) to 2.01 eV (617 nm)). It has been argued that the broad photoluminescence (PL) emission is associated with a high level of bond length distortion of the structure.<sup>16,50</sup> It is noteworthy to draw comparison to the published structure of the lead iodide analogues. The 2D (pPDA)PbI<sub>4</sub> cannot be stabilized with pPDA cation, but the synthesis and photo-physical characterization of 2D (mPDA)PbI<sub>4</sub> were previously reported in our group.<sup>51</sup> Although the average Pb-I-Pb angle for 2D (mPDA)PbI<sub>4</sub> is 143.8°, similar to that in (mPDA)PbBr<sub>4</sub> (Table 2), the bond length distortion of the octahedron in 2D (mPDA)PbI<sub>4</sub> is smaller than in (mPDA)PbBr<sub>4</sub>. This could be linked to the narrower PL emission of 2D (mPDA)PbI<sub>4</sub> than that of (mPDA)PbBr<sub>4</sub>.

The 1D (oPDA)<sub>4</sub>(PbBr<sub>4</sub>)<sub>2</sub>Pb<sub>3</sub>Br<sub>10</sub>•4H<sub>3</sub>PO<sub>2</sub> compound exhibits a narrow PL peak at 2.58 eV with an FWHM of 0.62 eV. The optical properties of the 1D (oPDA)<sub>2</sub>Pb<sub>3</sub>Br<sub>10</sub> structures are shown in Figures S2–S3. The broad PL emission for 1D (oPDA)<sub>2</sub>Pb<sub>3</sub>Br<sub>10</sub> might be attributed to the relatively larger bond length distortion than 1D (oPDA)<sub>4</sub>(PbBr<sub>4</sub>)<sub>2</sub>Pb<sub>3</sub>Br<sub>10</sub>•4H<sub>3</sub>PO<sub>2</sub>. From time-resolved PL experiments (Figure 6c), we observe that the average lifetimes for 2D (pPDA)PbBr<sub>4</sub>, 2D (mPDA)PbBr<sub>4</sub>, and 1D (oPDA)<sub>4</sub>(PbBr<sub>4</sub>)<sub>2</sub>Pb<sub>3</sub>Br<sub>10</sub>•4H<sub>3</sub>PO<sub>2</sub> are 3.05 ns, 3.17 ns, and 1.72 ns, respectively (Table 3), which is an indication of slower carrier recombination and improved carrier transport for 2D compounds compared to the 1D system.<sup>52</sup> The measured average lifetime of each sample was fitted using a three-exponent function (details are provided in the experimental section). To further explore the mechanism of the broadband emission, we performed variable-temperature PL from 80 K to 290 K for 2D (mPDA)PbBr<sub>4</sub> and (pPDA)PbBr<sub>4</sub> compounds (Figure S4). Both the PL spectra present a significant red shift, decreased PL intensity and broadening of the PL peak with increasing temperature. Thus, trap-mediated excitonic recombination or self-trapped excitons (STEs) might also contribute to the broadband emission.<sup>54,58,59</sup>

**Table 3** | Summary of PL average lifetimes for 2D (pPDA)PbBr<sub>4</sub>, 2D (mPDA)PbBr<sub>4</sub>, 1D (oPDA)<sub>4</sub>(PbBr<sub>4</sub>)<sub>2</sub>Pb<sub>3</sub>Br<sub>10</sub>•4H<sub>3</sub>PO<sub>2</sub> with estimated standard deviations in parentheses.

	$\tau_1$	$\tau_2$	$\tau_3$	$\tau_{\text{average}}$
(pPDA)PbBr <sub>4</sub>	0.98	3.07	12.87	3.17 ns
(mPDA)PbBr <sub>4</sub>	0.99	3.08	15.89	3.05 ns
(oPDA) <sub>4</sub> (PbBr <sub>4</sub> ) <sub>2</sub> Pb <sub>3</sub> Br <sub>10</sub> •4H <sub>3</sub> PO <sub>2</sub>	0.78	2.27	8.99	1.72 ns
(pPDA)PbBr <sub>4</sub> film	0.67	3.01	19.57	3.16 ns
(mPDA)PbBr <sub>4</sub> film	0.81	2.75	15.82	1.93 ns
(oPDA) <sub>4</sub> (PbBr <sub>4</sub> ) <sub>2</sub> Pb <sub>3</sub> Br <sub>10</sub> •4H <sub>3</sub> PO <sub>2</sub> film	0.73	2.64	20.23	1.88 ns

These low-dimensional perovskites with short rigid conjugated spacer dications can achieve large-scale tunability in the chromaticity of emission. The chromaticity diagram (CIE) and correlated color temperature (CCT) are obtained using the color calculator software (OSRAM Sylvania, Inc.), as shown in **Figure 7**. Their coordinates deviate from the white point (0.33, 0.33) as shown in **Table 2**.<sup>53</sup> The photos of light emissive samples are captured under UV illumination (TOC). The CCT below 4500 K can produce neutral to warm-white light. The (mPDA)PbBr<sub>4</sub> has a CIE coordinate of (0.44, 0.46), which has a reddish-white emission compared to the white point at (0.33, 0.33). The CIE of (pPDA)PbBr<sub>4</sub> and 1D (oPDA)<sub>4</sub>(PbBr<sub>4</sub>)<sub>2</sub>Pb<sub>3</sub>Br<sub>10</sub>•4H<sub>3</sub>PO<sub>2</sub> are (0.34, 0.44) and (0.21, 0.29), respectively, and they give CCT of 5450 K and >10000 K, respectively. Thus, they emit cold-white light.

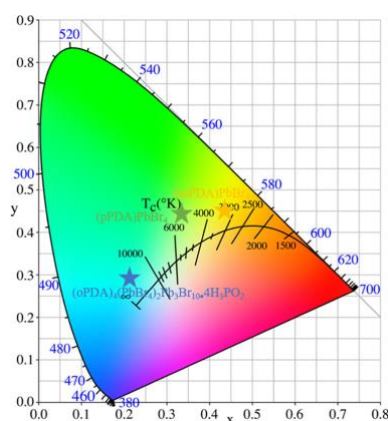


**Figure 7** | CIE color coordinates of (pPDA)PbBr<sub>4</sub>, (mPDA)PbBr<sub>4</sub>, (oPDA)<sub>4</sub>(PbBr<sub>4</sub>)<sub>2</sub>Pb<sub>3</sub>Br<sub>10</sub>•4H<sub>3</sub>PO<sub>2</sub> in 1931 color space chromaticity diagram. The chromaticity coordinates (x, y), CCT, and CRI are calculated using the Color Calculator software (OSRAM Sylvania, Inc).

Considering these newly synthesized perovskite compounds could be used in future devices, it is important to know the energy positions of their valence and conduction bands in terms of the correct interface and device assembly. The valence band maximum (VBM) of the different compounds was measured by photoemission yield spectroscopy in air (PYS) (**Figure 8a-d**). Here we should mention that the conduction band minimum (CBM) is calculated from the difference between the VBM and the band-gap. There might be an underestimation on the order of a few hundreds of meV due to the existence of exciton binding energy in the 2D perovskite material.<sup>54</sup> We also compare the VBM and CBM of the three compounds with those of PbBr<sub>2</sub> and 3D MAPbBr<sub>3</sub> perovskite.<sup>19</sup> The three compounds have a strong energy variation in the CBM (2.57 eV for (pPDA)PbBr<sub>4</sub>, 2.51 eV for (pPDA)PbBr<sub>4</sub>, and 2.04 eV for 1D (oPDA)<sub>4</sub>(PbBr<sub>4</sub>)<sub>2</sub>Pb<sub>3</sub>Br<sub>10</sub>•4H<sub>3</sub>PO<sub>2</sub>), whereas the VBMs (5.49 eV for (pPDA)PbBr<sub>4</sub>, 5.54 eV for (pPDA)PbBr<sub>4</sub>, and 5.52 eV for 1D (oPDA)<sub>4</sub>(PbBr<sub>4</sub>)<sub>2</sub>Pb<sub>3</sub>Br<sub>10</sub>•4H<sub>3</sub>PO<sub>2</sub>) remain almost constant. Compared with those of PbBr<sub>2</sub> and 3D MAPbBr<sub>3</sub>, the VBM for the three compounds are similar to that of 3D MAPbBr<sub>3</sub>, while the VBM for the three compounds are between those of PbBr<sub>2</sub> and 3D MAPbBr<sub>3</sub>. Thus, the different cations significantly influence the VBM and CBM, which is an important factor for the correct interface assembly.

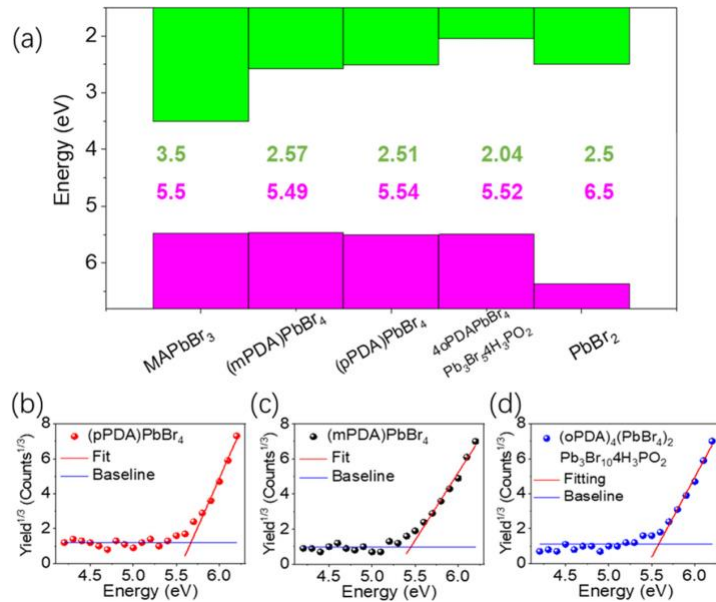


**Figure 8** | (a) Experimental energy band alignment (VBM and CBM) of lead bromide compounds of (pPDA)PbBr<sub>4</sub>, (mPDA)PbBr<sub>4</sub>, and (oPDA)<sub>4</sub>(PbBr<sub>4</sub>)<sub>2</sub>Pb<sub>3</sub>Br<sub>10</sub>•4H<sub>3</sub>PO<sub>2</sub> compared with that of the 3D MAPbBr<sub>3</sub> and PbBr<sub>2</sub>. Work function measurement for (b) 2D (pPDA)PbBr<sub>4</sub>, (c) 2D (mPDA)PbBr<sub>4</sub>, (d) 1D (oPDA)<sub>4</sub>(PbBr<sub>4</sub>)<sub>2</sub>Pb<sub>3</sub>Br<sub>10</sub>•4H<sub>3</sub>PO<sub>2</sub>, respectively.

## 2.5. Electronic Band Structure Calculations

The electronic band structures of (pPDA)PbBr<sub>4</sub> and (mPDA)PbBr<sub>4</sub> are shown in **Figure 9a-b**. Both 2D materials are direct-band-gap semiconductors at the  $\Gamma$  point of the Brillouin zone. Employing the hybrid functional PBE0, which is known to correct the DFT underestimated band-gap values,<sup>55,56</sup> we calculated the electronic band-gaps of 3.40 eV for (pPDA)PbBr<sub>4</sub> and (mPDA)PbBr<sub>4</sub>, slightly larger than the 3.11 eV electronic band-gap of the prototypical Ruddlesden-Popper layered perovskite (BA)<sub>2</sub>PbBr<sub>4</sub>. For 1D (oPDA)<sub>4</sub>(PbBr<sub>4</sub>)<sub>2</sub>Pb<sub>3</sub>Br<sub>10</sub>•4H<sub>3</sub>PO<sub>2</sub>, the band-gap is indirect (**Figure S5**), and larger (4.11 eV within PBE0) than the 2D materials, in agreement with the experiments. The difference between the calculated band-gaps matches the trend observed in the optical absorption spectra (*vide infra*). As expected, the Pb s-orbitals and Br p-orbitals contribute to the VBM, while the conduction band minimum (CBM) is composed of mainly Pb p-orbitals (**Figure S6**). The organic spacer layers, whose states are shown by flat non-dispersive bands (**Figure 9a-c**), do not contribute to the band edges; However, for the 2D compounds, a few organic electronic states are found above the CBM, in contrast to the reference 2D compound (BA)<sub>2</sub>PbBr<sub>4</sub>.<sup>57</sup>

The out-of-plane interactions between halogens of adjacent inorganic slabs of 2D perovskite materials are known to play a crucial role in the electronic band structure, especially in iodides.<sup>60,61</sup> To quantify this effect, we calculated the VBM and CBM band dispersion along the stacking direction for the 2D materials, as shown in green in **Figure 9**. For the VBM of (pPDA)PbBr<sub>4</sub> and (mPDA)PbBr<sub>4</sub>, we found small dispersions of 110 meV and 83 meV, respectively, while for the CBM 18 meV and 21 meV, within the DFT-PBE0. This is not the case for (BA)<sub>2</sub>PbBr<sub>4</sub>, for which the dispersion is 0 because the apical interlayer bromines are too far away to interact.

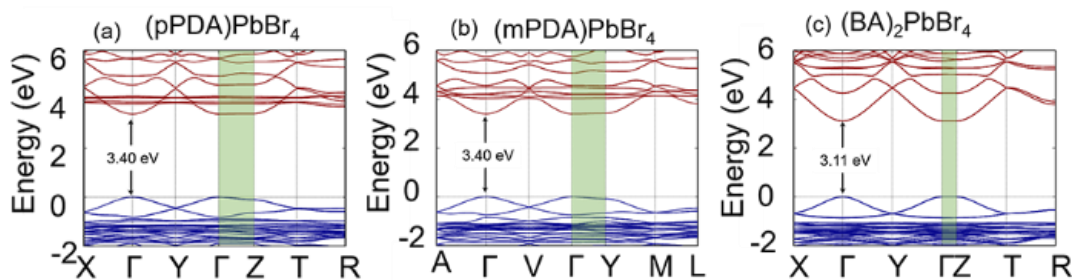


**Figure 9** | Electronic structure for the 2D compounds (a) (pPDA)PbBr<sub>4</sub>, (b) (mPDA)PbBr<sub>4</sub>, and prototypical layered perovskite (c) (BA)<sub>2</sub>PbBr<sub>4</sub>. The band-gap is calculated employing the hybrid exchange-correlation functional PBE0. The direction that corresponds to the layer stacking is highlighted in green.

Finally, to explore the intralayer charge carrier transport of the 2D materials, we calculated their in-plane effective masses for holes and electrons and compared them to those of (BA)<sub>2</sub>PbBr<sub>4</sub>. The effective masses of (pPDA)PbBr<sub>4</sub> and (mPDA)PbBr<sub>4</sub> are found slightly larger,  $m_e = 0.36$  and  $0.34$  and  $m_h = 0.53$  and  $0.50 m_0$ , than those for (BA)<sub>2</sub>PbBr<sub>4</sub>,  $m_e = 0.19$  and  $m_h = 0.33 m_0$ . This observation is consistent with the larger in-plane distortions of the Pb-Br octahedra.

Our results show that the here-observed distortions of layered halide perovskites tend to increase the bandgap and the in-plane hole and electron effective masses. Yet, we find no direct relation between the electronic band structure of the compounds and their emission. Hence, the existence of low-energy white-light emission, and its observed correlation with structural distortions are not originating from the electronic structures of (pPDA)PbBr<sub>4</sub> and (mPDA)PbBr<sub>4</sub>. Other possible physical mechanisms underlying the observed emission, and can be further explored, such as exciton trapping facilitated by the strong distortions in the inorganic parts of the structures, as hinted by the results of the temperature-dependent PL spectra of (pPDA)PbBr<sub>4</sub> and (mPDA)PbBr<sub>4</sub> (Figure S4).

## 2.6. Film Properties and Stability

Most perovskite films reported previously were made from mixtures of the precursor components.<sup>62</sup> Herein, we dissolve the single crystals directly in the solvent, and the memory seeds could enable high structural phase purity in the 2D perovskite film.<sup>63</sup> Notably, the (pPDA)PbBr<sub>4</sub> compounds form a clear N,N-DMF solution, but a dark blue solution forms in dimethyl sulfoxide (DMSO). The 2D (pPDA)PbBr<sub>4</sub> cannot dissolve in acetonitrile (ACN) and gamma-butyrolactone (GBL) (Figure S7). Thus, all three crystals are dissolved in anhydrous DMF. The details of the film assembly are described in the experimental section.

The XRD patterns of the films (Figure 10a) exhibit low-angle basal Bragg peaks below  $2\theta = 10^\circ$ , similar to the powder XRD pattern of single-crystal materials. The optical absorption spectra (Figure 10b) confirm the formation of 2D perovskite pure phases for (pPDA)PbBr<sub>4</sub> and (mPDA)PbBr<sub>4</sub> films. For 1D (oPDA)<sub>4</sub>PbBr<sub>4</sub>Pb<sub>3</sub>Br<sub>5</sub>·4H<sub>3</sub>PO<sub>2</sub>, the absorption edge is 3.45 eV, which is also similar to the material itself. The PL from the 2D (pPDA)PbBr<sub>4</sub> and (mPDA)PbBr<sub>4</sub> films still show broad emission (Figure 10c). In addition, all the average lifetimes are comparable to the bulk materials at 1.93 ns, 3.17 ns, and 1.88 ns for 2D

(pPDA)PbBr<sub>4</sub>, 2D (mPDA)PbBr<sub>4</sub>, and 1D (oPDA)<sub>4</sub>(PbBr<sub>4</sub>)<sub>2</sub>Pb<sub>3</sub>Br<sub>10</sub>•4H<sub>3</sub>PO<sub>2</sub> films, respectively (Figure 10d and Table 3).

We also investigated the stability of the three-hybrid lead bromide perovskite films to assess their potential in devices (Figure S8). We used a continuous UV irradiation illumination test in the air (temperature, 22 °C; humidity, 35%). All the color and XRD results for the three films remain constant for more than 24 h. The long-term thermal stability test was conducted on a hot plate at 80 °C in the air (temperature 22 °C, humidity 35%). According to the XRD results, only the (mPDA)PbBr<sub>4</sub> films remain stable during continuous heating in air for more than 24 h. We find splitting in the low-angle ( $2\theta < 10^\circ$ ) Bragg peaks for the other two cases, suggesting the structural decomposition. The color for the (pPDA)PbBr<sub>4</sub> films changes from white to dark grey, and light pink for the 1D (oPDA)<sub>4</sub>(PbBr<sub>4</sub>)<sub>2</sub>Pb<sub>3</sub>Br<sub>10</sub>•4H<sub>3</sub>PO<sub>2</sub> films, after 24 h heating in air. Thus, the (mPDA)PbBr<sub>4</sub> films exhibit the best thermal stability due to the stronger hydrogen-bonding interactions in its structure.

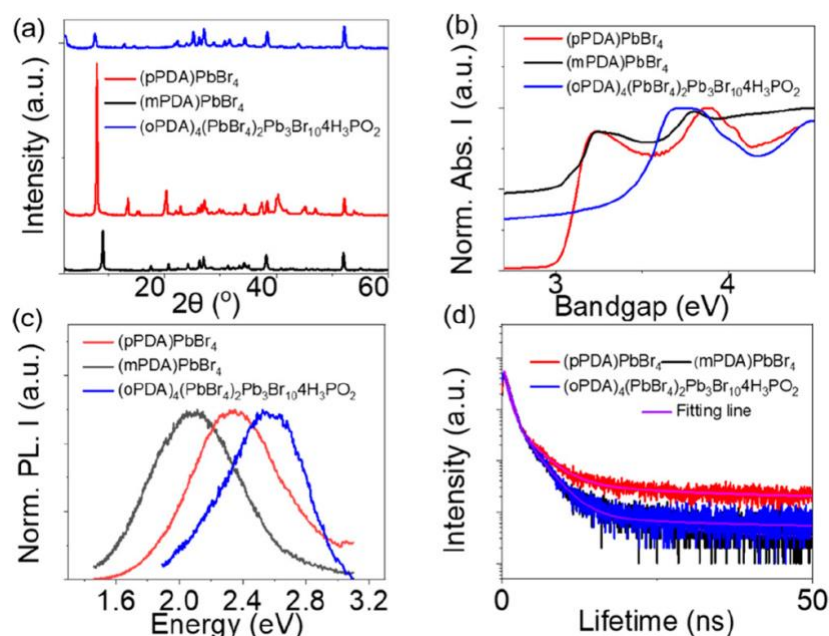


**Figure 10** | (a) PXRD patterns, (b) Optical absorption spectra, (c) steady-state PL spectra, and (d) time-resolved PL spectra for 2D (pPDA)PbBr<sub>4</sub>, 2D (mPDA)PbBr<sub>4</sub>, 1D (oPDA)<sub>4</sub>(PbBr<sub>4</sub>)<sub>2</sub>Pb<sub>3</sub>Br<sub>10</sub>•4 H<sub>3</sub>PO<sub>2</sub> films, respectively.

### 3. Conclusions

The influence of ammonium group positions in the short rigid aromatic moiety of phenylene diammonium family on the crystal structures of low-dimensional lead bromides is strong and leads to 2D perovskite and 1D non-perovskite motifs all with broad white-light emission. When the amino groups are in the meta and para positions, the aromatic diammonium cations allow the formation of 2D network perovskite structures ( $n=1$ ). When in the ortho positions, the cations stabilize only 1D structures. New insights into the local packing arrangements of organic spacers and organic-inorganic interfaces are obtained using high-field <sup>1</sup>H and <sup>207</sup>Pb solid-state 2D-NMR spectroscopy. The (pPDA)PbBr<sub>4</sub> and (mPDA)PbBr<sub>4</sub>

perovskite exhibit different ammonium group penetrations and hydrogen-bonding interactions, which modulate the Br-Pb-Br bond angles and the tilting of the corner-sharing  $\text{PbBr}_6$  octahedra. The NMR shows large difference in the  $^{207}\text{Pb}$  ( $\delta$  ~100 ppm) and  $^1\text{H}$  chemical shifts of the  $-\text{NH}_3^+$  groups ( $\delta$  ~0.5 ppm), among the compounds reflecting the local  $\text{PbBr}_6$  distortions. We also find structure-PL correlations, which link the level of the bond length distortions in the inorganic  $[\text{PbBr}_4]^{2-}$  layer to the broad bandwidth of the PL emission. The bond length distortions for the three compounds in descending order are 2D (mPDA) $\text{PbBr}_4$  > 2D (pPDA) $\text{PbBr}_4$  > 1D (oPDA) $_4\text{PbBr}_4\text{Pb}_3\text{Br}_5 \cdot 4\text{H}_3\text{PO}_2$ . Consequently, 2D (mPDA) $\text{PbBr}_4$  compounds exhibit the broadest white light emission, while the narrowest white emission is observed for 1D (oPDA) $_4\text{PbBr}_4\text{Pb}_3\text{Br}_5 \cdot 4\text{H}_3\text{PO}_2$ . Density functional theory calculations for 2D (mPDA) $\text{PbBr}_4$  and 2D (pPDA) $\text{PbBr}_4$  suggests direct band-gaps with relatively broad valence and conduction bands along the in-plane directions, but a slightly indirect band-gap for the 1D (oPDA) $_4\text{PbBr}_4\text{Pb}_3\text{Br}_5 \cdot 4\text{H}_3\text{PO}_2$ . The (mPDA) $\text{PbBr}_4$  film exhibits better thermal stability in ambient air than the other two films, presumably because of the stronger hydrogen-bonding interactions in the material. Therefore, our findings support the general belief that tuning the structural distortion in low-dimensional perovskites based on the shape and size of the spacer cation is an effective handle for designing single-source white-light emitters.

#### 4. Experimental section

##### 4.1. Synthesis of 2D (pPDA) $\text{PbBr}_4$ , 2D (mPDA) $\text{PbBr}_4$ , 1D (oPDA) $_4(\text{PbBr}_4)_2\text{Pb}_3\text{Br}_{10} \cdot 4 \text{H}_3\text{PO}_2$ and 1D (oPDA) $_2\text{Pb}_3\text{Br}_{10}$

- 4.1.1. For (pPDA) $\text{PbBr}_4$   $n = 1$ . 446.4 mg (2 mmol) of  $\text{PbO}$  powder was dissolved in 5 mL of hydrobromic acid and 1 mL of  $\text{H}_3\text{PO}_2$  solution (or without 1 mL of  $\text{H}_3\text{PO}_2$ ) by heating, with constant stirring for 5–10 min at  $\sim 200^\circ\text{C}$  until the solution became clear. Then 64.9 mg (0.6 mmol) of pPDA was added directly to the above solution under the same conditions until complete dissolution. Finally, the solution was cooled to  $120^\circ\text{C}$  and eventually to room temperature to obtain white plate-like crystals of pPDAPbBr<sub>4</sub>. The product was isolated by suction filtration followed by drying in a filtration funnel for 30 min. The yield obtained was 750 mg (58.9% of total Pb content).
- 4.1.2. For (mPDA) $\text{PbBr}_4$   $n = 1$ . 446.4 mg (2 mmol) of  $\text{PbO}$  powder was dissolved in 3 mL of hydrobromic acid and 1 mL of  $\text{H}_3\text{PO}_2$  solution (or without 1 mL of  $\text{H}_3\text{PO}_2$ ) by heating with constant stirring for 5–10 min at  $\sim 200^\circ\text{C}$  until the solution became clear. Then 64.9 mg (0.6 mmol) of mPDA was added directly to the above solution under the same conditions until complete dissolution. Finally, the solution was cooled to  $120^\circ\text{C}$  and eventually to room temperature to obtain white plate-like crystals of mPDAPbBr<sub>4</sub>. The product was isolated by suction filtration followed by drying in a filtration funnel for 30 min. Yield obtained was 366 mg (28.7% of the total Pb content).

4.1.3. For  $(\text{oPDA})_4(\text{PbBr}_4)_2\text{Pb}_3\text{Br}_{10}\cdot 4\text{H}_3\text{PO}_2$ . 446.4 mg (2 mmol) of PbO powder was dissolved in 3 mL of hydrobromic acid and 1 mL of  $\text{H}_3\text{PO}_2$  solution by heating with constant stirring for 5–10 min at  $\sim 200$  °C until the solution became clear. The only difference for 1D  $(\text{oPDA})_4\text{Pb}_3\text{Br}_{10}$  was the absence of 1 mL of  $\text{H}_3\text{PO}_2$ . Next, 64.9 mg (0.6 mmol) of oPDA was added directly to the above solution with the same conditions until complete dissolution. Finally, the solution was cooled to 120 °C, and crystals were obtained at room temperature. The product was isolated by suction filtration followed by drying in a filtration funnel for 30 min. Yield obtained was 186 mg (14.6% of total Pb content).

**4.2. Film Fabrication.** FTO glass substrates were first cleaned by sequential sonication in acetone and isopropanol for 15 min each. Subsequently, the FTO substrates were dried with nitrogen and treated for 30 min using ultraviolet ozone (UVO). Solutions of the studied materials were prepared by dissolving 100 mg of dried crystals in 200  $\mu\text{L}$  of anhydrous DMF solvent. The substrates were heated at 110 °C on a hot plate for 10 min under  $\text{N}_2$  atmosphere. Then, the precursor solution was spin-coated at 5000 rpm for 30 s in a glovebox under a  $\text{N}_2$  atmosphere.

**4.3. Single-Crystal X-ray Crystallography:** Single-crystal XRD experiments were performed using a STOE IPDS II or IPDS 2T diffractometer with Mo  $\text{K}\alpha$  radiation ( $\lambda = 0.71073$  Å) operating at 50 kV and 40 mA. Integration and numerical absorption corrections were performed using X-AREA, X-RED, and XSHAPE programs. The structures were solved by charge flipping and refined using the full-matrix least-squares in Olex2. The PLATON software was used to identify the twinning domains and validate the space groups of the compounds.

**4.4. Solid-state NMR spectroscopy.** All solid-state magic-angle spinning (MAS) NMR experiments were carried out using an 18.8 T ( $^1\text{H}$ , 800.1 MHz) Bruker Avance Neo NMR spectrometer equipped with a 1.3-mm H-X probe head. Single-crystal samples of the 1D and 2D perovskites and precursor salts were separately packed into 1.3 mm zirconia rotors (outer diameter) fitted with VESPEL<sup>®</sup> caps. Unless otherwise specified, all the samples were spun at a MAS frequency of 50 kHz.  $^1\text{H}$  relaxation delays were determined from the saturation recovery measurements and analyses. Single-pulse  $^1\text{H}$  MAS NMR spectra were acquired by co-addition of 32 transients. The 1D  $^{207}\text{Pb}$  MAS experiments were carried out using a spin-echo pulse sequence. Each spectrum was acquired with 4096 co-added transients using a relaxation delay of 800 ms. For all compounds, 2D  $^1\text{H}$ - $^1\text{H}$  double-quantum (DQ)-single-quantum (SQ) NMR spectra were acquired using a back-to-back sequence under fast MAS.<sup>64</sup> A rotor-synchronized  $t_1$  increment of 20  $\mu\text{s}$  was applied with a DQ excitation time of 40  $\mu\text{s}$  corresponding to two rotor periods ( $2\tau_r$ ). The  $^1\text{H}$  DQ dimensions were acquired using 128  $t_1$  FIDs, each with 16 co-added transients. The  $^1\text{H}$  experimental spectra were calibrated with respect to that

of neat TMS using adamantane as an external reference ( $^1\text{H}$  resonance, 1.82 ppm).  $^{207}\text{Pb}$  experimental shift was calibrated with respect to neat liquid  $\text{Pb}(\text{NO}_3)_2$  based on IUPAC recommendation.

### **Author contributions**

P. Fu and M. Quintero contributed equally to this work. P. Fu performed sample synthesis, structural characterization, and optical measurements, and wrote the paper. M. Quintero and V. Klepov helped refine the single-crystal structure. C. W and G. N. M. Reddy carried out the solid-state NMR measurements and analyses. B. Cucco, G. Volonakis, J. Even, M. Kepenekian, and R. Liu performed density functional theory calculations. M.D. Siena trained the PL instrument, and Y. Liu and V. Dravid performed the SEM analyses. C. Laing performed the work function test. X. Li discussed the synthesis and revised the manuscript accordingly. C. Li revised the manuscript. M.G.K. supervised the study and revised the manuscript. The manuscript reflects the contributions of all the authors.

### **Acknowledgments**

This work was supported by the National Science Foundation under Grant No. DMR-2019444 (IMOD an NSF-STC). This work used the NUFAB facility of Northwestern University's NUANCE Center, which has received support from the SHyNE Resource (NSF ECCS-2025633), the IIN, and the Northwestern MRSEC program (NSF DMR-1720139). The MRSEC program (NSF DMR-1720139) at the Materials Research Center, the International Institute for Nanotechnology (IIN), the Keck Foundation, and the State of Illinois through IIN. GNMR gratefully acknowledges financial support from ISITE international mobility grant, IR INFRANALYTICS FR2054, and EU H2020 (Grant 795091) for conducting the ssNMR experiments. P. Fu acknowledges the financial support from the Chinese Academy of Science as a visiting scholar at Northwestern University, USA, 2020RQ036, and fruitful discussion with Chenjian Lin, Yanfeng Yin, and Paige Brown.

### **Supporting Information**

Additional experimental details, materials, and methods; The calculated/experimental XRD patterns, Optical absorption spectra, Steady-state PL spectra and Projected density of states (PDOS) and detailed single-crystal information for all compounds; Electronic structure for the 1D compounds; Temperature-dependent photoluminescence spectra for 2D compounds; Film stability of all compounds, including photographs of different solution.

### **Accession Codes**

CCDC 2182661-2182664 contain the supplementary crystallographic data for this paper.

## References

1. Fu, P.; Qin, W.; Bai, S. Q.; Yang, D.; Chen, L. D.; Guo, X.; Li, C., Integrating large-area perovskite solar module with thermoelectric generator for enhanced and stable power output. *Nano Energy* **2019**, *65*, 104009.
2. Yang, W. S.; Park, B. W.; Jung, E. H.; Jeon, N. J.; Kim, Y. C.; Lee, D. U.; Shin, S. S.; Seo, J.; Kim, E. K.; Noh, J. H.; Seok, S. I., Iodide management in formamidinium-lead-halide-based perovskite layers for efficient solar cells. *Science* **2017**, *356* (6345), 1376-1381.
3. Correa-Baena, J. P.; Saliba, M.; Buonassisi, T.; Gratzel, M.; Abate, A.; Tress, W.; Hagfeldt, A., Promises and challenges of perovskite solar cells. *Science* **2017**, *358* (6364), 739-744.
4. Kojima, A.; Teshima, K.; Shirai, Y.; Miyasaka, T., Organometal Halide Perovskites as Visible-Light Sensitizers for Photovoltaic Cells. *J Am Chem Soc* **2009**, *131* (17), 6050-6055.
5. Stranks, S. D.; Snaith, H. J., Metal-halide perovskites for photovoltaic and light-emitting devices. *Nat Nanotechnol* **2015**, *10* (5), 391-402.
6. Yuan, M. J.; Quan, L. N.; Comin, R.; Walters, G.; Sabatini, R.; Voznyy, O.; Hoogland, S.; Zhao, Y. B.; Beauregard, E. M.; Kanjanaboos, P.; Lu, Z. H.; Kim, D. H.; Sargent, E. H., Perovskite energy funnels for efficient light-emitting diodes. *Nat Nanotechnol* **2016**, *11* (10), 872-876.
7. Stoumpos, C. C.; Malliakas, C. D.; Kanatzidis, M. G., Semiconducting Tin and Lead Iodide Perovskites with Organic Cations: Phase Transitions, High Mobilities, and Near-Infrared Photoluminescent Properties. *Inorg Chem* **2013**, *52* (15), 9019-9038.
8. Ahmad, S.; Fu, P.; Yu, S. W.; Yang, Q.; Liu, X.; Wang, X. C.; Wang, X. L.; Guo, X.; Li, C., Dion-Jacobson Phase 2D Layered Perovskites for Solar Cells with Ultrahigh Stability (vol 3, pg 794, 2019). *Joule* **2019**, *3* (3), 889-890.
9. Tsai, H. H.; Nie, W. Y.; Blancon, J. C.; Toumpos, C. C. S.; Asadpour, R.; Harutyunyan, B.; Neukirch, A. J.; Verduzco, R.; Crochet, J. J.; Tretiak, S.; Pedesseau, L.; Even, J.; Alam, M. A.; Gupta, G.; Lou, J.; Ajayan, P. M.; Bedzyk, M. J.; Kanatzidis, M. G.; Mohite, A. D., High-efficiency two-dimensional Ruddlesden-Popper perovskite solar cells. *Nature* **2016**, *536* (7616), 312-318.
10. Li, X. T.; Hoffman, J. M.; Kanatzidis, M. G., The 2D Halide Perovskite Rulebook: How the Spacer Influences Everything from the Structure to Optoelectronic Device Efficiency. *Chem Rev* **2021**, *121* (4), 2230-2291.
11. Mao, L. L.; Ke, W. J.; Pedesseau, L.; Wu, Y. L.; Katan, C.; Even, J.; Wasielewski, M. R.; Stoumpos, C. C.; Kanatzidis, M. G., Hybrid Dion-Jacobson 2D Lead Iodide Perovskites. *J Am Chem Soc* **2018**, *140* (10), 3775-3783.
12. Ke, W. J.; Mao, L. L.; Stoumpos, C. C.; Hoffman, J.; Spanopoulos, I.; Mohite, A. D.; Kanatzidis, M. C., Compositional and Solvent Engineering in Dion-Jacobson 2D Perovskites Boosts Solar Cell Efficiency and Stability. *Adv Energy Mater* **2019**, *9* (10), 1803384.
13. Li, W. B.; Sidhik, S.; Traore, B.; Asadpour, R.; Hou, J.; Zhang, H.; Fehr, A.; Essman, J.; Wang, Y. F.; Hoffman, J. M.; Spanopoulos, I.; Crochet, J. J.; Tsai, E.; Strzalka, J.; Katan, C.; Alam, M. A.; Kanatzidis, M. G.; Even, J.; Blancon, J. C.; Mohite, A. D., Light-activated interlayer contraction in two-dimensional perovskites for high-efficiency solar cells. *Nat Nanotechnol* **2022**, *17* (1), 45-50.
14. Qian, J. Y.; Guo, Q.; Liu, L. J.; Xu, B.; Tian, W. J., A theoretical study of hybrid lead iodide perovskite homologous semiconductors with 0D, 1D, 2D and 3D structures. *J Mater Chem A* **2017**, *5* (32), 16786-16795.
15. Dohner, E. R.; Hoke, E. T.; Karunadasa, H. I., Self-Assembly of Broadband White-Light Emitters. *J Am Chem Soc* **2014**, *136* (5), 1718-1721.
16. Mao, L. L.; Wu, Y. L.; Stoumpos, C. C.; Wasielewski, M. R.; Kanatzidis, M. G., White-Light Emission and Structural Distortion in New Corrugated Two-Dimensional Lead Bromide Perovskites. *J Am Chem Soc* **2017**, *139* (14), 5210-5215.
17. Thirumal, K.; Chong, W. K.; Xie, W.; Ganguly, R.; Muduli, S. K.; Sherburne, M.; Asta, M.; Mhaisalkar, S.; Sum, T. C.; Soo, H. S.; Mathews, N., Morphology-Independent Stable White-Light Emission from Self-Assembled Two-Dimensional Perovskites Driven by Strong Exciton-Phonon Coupling to the Organic Framework. *Chem Mater* **2017**, *29* (9), 3947-3953.
18. Guo, Y. Y.; Yang, L. J.; Biberger, S.; McNulty, J. A.; Li, T.; Schotz, K.; Panzer, F.; Lightfoot, P., Structural Diversity in Layered Hybrid Perovskites, A(2)PbBr(4) or AA'PbBr4, Templated by Small Disc-Shaped Amines. *Inorg Chem* **2020**, *59* (17), 12858-12866.
19. Mao, L. L.; Guo, P. J.; Kepenekian, M.; Hadar, I.; Katan, C.; Even, J.; Schaller, R. D.; Stoumpos, C. C.; Kanatzidis, M. G., Structural Diversity in White-Light-Emitting Hybrid Lead Bromide Perovskites. *J Am Chem Soc* **2018**, *140* (40), 13078-13088.
20. Yuan, Z.; Zhou, C. K.; Tian, Y.; Shu, Y.; Messier, J.; Wang, J. C.; van de Burgt, L. J.; Kountouriotis, K.; Xin, Y.; Holt, E.; Schanze, K.; Clark, R.; Siegrist, T.; Ma, B. W., One-dimensional organic lead halide perovskites with efficient bluish white-light emission. *Nat Commun* **2017**, *8*, 14051.
21. Lin, H. R.; Zhou, C. K.; Tian, Y.; Siegrist, T.; Ma, B. W., Low-Dimensional Organometal Halide Perovskites. *Acs Energy Lett* **2018**, *3* (1), 54-62.

22. Zhao, S. Y.; Jiang, S. Q.; Cai, W. S.; Li, R.; Mo, Q. H.; Wang, B. Q.; Zang, Z. G., Intrinsic white-light emission from low-dimensional perovskites for white-light-emitting diodes with high-color-rendering index. *Cell Rep Phys Sci* **2021**, *2* (10), 100585.
23. Sun, S. Q.; Lu, M.; Gao, X. P.; Shi, Z. F.; Bai, X.; Yu, W. W.; Zhang, Y., OD Perovskites: Unique Properties, Synthesis, and Their Applications. *Adv Sci* **2021**, *8* (24), 2102689.
24. Yantara, N.; Bruno, A.; Iqbal, A.; Jamaludin, N. F.; Soci, C.; Mhaisalkar, S.; Mathews, N., Designing Efficient Energy Funneling Kinetics in Ruddlesden-Popper Perovskites for High-Performance Light-Emitting Diodes. *Adv Mater* **2018**, *30* (33), 1800818.
25. Shi, Y. M.; Hu, J. R.; Chen, J.; Xu, Y. X.; Yang, W. T.; Chen, J. N.; He, Y. B., 5-Ammoniumvaleric acid stabilized mixed-dimensional perovskite submicron platelets with white light emission. *Nanoscale Adv* **2020**, *2* (10), 4822-4829.
26. Kennard, R. M.; Dahlman, C. J.; Chung, J.; Cotts, B. L.; Mikhailovsky, A. A.; Mao, L. L.; DeCrescent, R. A.; Stone, K. H.; Venkatesan, N. R.; Mohtashami, Y.; Assadi, S.; Salleo, A.; Schuller, J. A.; Seshadri, R.; Chabinyk, M. L., Growth-Controlled Broad Emission in Phase-Pure Two-Dimensional Hybrid Perovskite Films. *Chem Mater* **2021**, *33* (18), 7290-7300.
27. Li, X.; Ke, W.; Traore, B.; Guo, P.; Hadar, I.; Kepenekian, M.; Even, J.; Katan, C.; Stoumpos, C. C.; Schaller, R. D.; Kanatzidis, M. G., Two-Dimensional Dion-Jacobson Hybrid Lead Iodide Perovskites with Aromatic Diammonium Cations. *J Am Chem Soc* **2019**, *141* (32), 12880-12890.
28. Shi, P. P.; Lu, S. Q.; Song, X. J.; Chen, X. G.; Liao, W. Q.; Li, P. F.; Tang, Y. Y.; Xiong, R. G., Two-Dimensional Organic-Inorganic Perovskite Ferroelectric Semiconductors with Fluorinated Aromatic Spacers. *J Am Chem Soc* **2019**, *141* (45), 18334-18340.
29. Gao, L.; Li, X.; Traore, B.; Zhang, Y.; Fang, J.; Han, Y.; Even, J.; Katan, C.; Zhao, K.; Liu, S.; Kanatzidis, M. G., m-Phenylenediammonium as a New Spacer for Dion-Jacobson Two-Dimensional Perovskites. *J Am Chem Soc* **2021**, *143* (31), 12063-12073.
30. Lemmerer, A.; Billing, D. G., Two packing motifs based upon chains of edge-sharing PbI<sub>6</sub> octahedra. *Acta Crystallogr C* **2006**, *62*, 597-601.
31. Mao, L. L.; Stoumpos, C. C.; Kanatzidis, M. G., Two-Dimensional Hybrid Halide Perovskites: Principles and Promises. *J Am Chem Soc* **2019**, *141* (3), 1171-1190.
32. Vasileiadou, E. S.; Wang, B.; Spanopoulos, I.; Hadar, I.; Navrotsky, A.; Kanatzidis, M. G., Insight on the Stability of Thick Layers in 2D Ruddlesden-Popper and Dion-Jacobson Lead Iodide Perovskites. *J Am Chem Soc* **2021**, *143* (6), 2523-2536.
33. Marchenko, E. I.; Korolev, V. V.; Mitrofanov, A.; Fateev, S. A.; Goodilin, E. A.; Tarasov, A. B., Layer Shift Factor in Layered Hybrid Perovskites: Univocal Quantitative Descriptor of Composition-Structure-Property Relationships. *Chem Mater* **2021**, *33* (4), 1213-1217.
34. Shibuya, K.; Koshimizu, M.; Nishikido, F.; Saito, H.; Kishimoto, S., Poly[bis(phenethyl-ammonium) [di-bromido-plumbate(II)]-di-mu-bromido]. *Acta Crystallogr Sect E Struct Rep Online* **2009**, *65*, 1323-1324.
35. Smith, M. D.; Jaffe, A.; Dohner, E. R.; Lindenberg, A. M.; Karunadasa, H. I., Structural origins of broadband emission from layered Pb-Br hybrid perovskites. *Chem Sci* **2017**, *8* (6), 4497-4504.
36. Janiak, C., A critical account on pi-pi stacking in metal complexes with aromatic nitrogen-containing ligands. *J Chem Soc Dalton* **2000**, (21), 3885-3896.
37. Lufaso, M. W.; Woodward, P. M., Jahn-Teller distortions, cation ordering and octahedral tilting in perovskites. *Acta Crystallogr B* **2004**, *60*, 10-20.
38. Alonso, J. A.; Martinez-Lope, M. J.; Casais, M. T.; Fernandez-Diaz, M. T., Evolution of the Jahn-Teller distortion of MnO<sub>6</sub> octahedra in RMnO<sub>3</sub> perovskites (R = Pr, Nd, Dy, Tb, Ho, Er, Y): A neutron diffraction study. *Inorg Chem* **2000**, *39* (5), 917-923.
39. Robinson, K.; Gibbs, G. V.; Ribbe, P. H., Quadriatic Elongation - Quantitative Measure of Distortion in Coordination Polyhedra. *Science* **1971**, *172* (3983), 567-572.
40. Lee, J. H.; Bristowe, N. C.; Bristowe, P. D.; Cheetham, A. K., Role of hydrogen-bonding and its interplay with octahedral tilting in CH<sub>3</sub>NH<sub>3</sub>PbI<sub>3</sub>. *Chem Commun* **2015**, *51* (29), 6434-6437.
41. Kubicki, D. J.; Stranks, S. D.; Grey, C. P.; Emsley, L., NMR spectroscopy probes microstructure, dynamics and doping of metal halide perovskites. *Nat Rev Chem* **2021**, *5* (9), 624-645.
42. Spanopoulos, I.; Hadar, I.; Ke, W. J.; Guo, P. J.; Mozur, E. M.; Morgan, E.; Wang, S. X.; Zheng, D.; Padgaonkar, S.; Reddy, G. N. M.; Weiss, E. A.; Hersam, M. C.; Seshadri, R.; Schaller, R. D.; Kanatzidis, M. G., Tunable Broad Light Emission from 3D "Hollow" Bromide Perovskites through Defect Engineering. *J Am Chem Soc* **2021**, *143* (18), 7069-7080.
43. Kazemi, M. A. A.; Raval, P.; Cherednichkno, K.; Chotard, J. N.; Krishna, A.; Demortiere, A.; Reddy, G. N. M.; Sauvage, F., Molecular-Level Insight into Correlation between Surface Defects and Stability of Methylammonium Lead Halide Perovskite Under Controlled Humidity. *Small Methods* **2021**, *5* (2), 2000834.

44. Krishna, A.; Zhang, H.; Zhou, Z. W.; Gallet, T.; Dankl, M.; Ouellette, O.; Eickemeyer, F. T.; Fu, F.; Sanchez, S.; Mensi, M.; Zakeeruddin, S. M.; Rothlisberger, U.; Reddy, G. N. M.; Redinger, A.; Gratzel, M.; Hagfeldt, A., Nanoscale interfacial engineering enables highly stable and efficient perovskite photovoltaics. *Energ Environ Sci* **2021**, *14* (10), 5552-5562.
45. Dahlman, C. J.; Kennard, R. M.; Paluch, P.; Venkatesan, N. R.; Chabiny, M. L.; Reddy, G. N. M., Dynamic Motion of Organic Spacer Cations in Ruddlesden-Popper Lead Iodide Perovskites Probed by Solid-State NMR Spectroscopy. *Chem Mater* **2021**, *33* (2), 642-656.
46. Piveteau, L.; Morad, V.; Kovalenko, M. V., Solid-State NMR and NQR Spectroscopy of Lead-Halide Perovskite Materials. *J Am Chem Soc* **2020**, *142* (46), 19413-19437.
47. Raval, P.; Kennard, R. M.; Vasileiadou, E. S.; Dahlman, C. J.; Spanopoulos, I.; Chabiny, M. L.; Kanatzidis, M.; Reddy, G. N. M., Understanding Instability in Formamidinium Lead Halide Perovskites: Kinetics of Transformative Reactions at Grain and Subgrain Boundaries. *Acs Energy Lett* **2022**, *7* (4), 1534-1543.
48. Stoumpos, C. C.; Kanatzidis, M. G., The Renaissance of Halide Perovskites and Their Evolution as Emerging Semiconductors. *Accounts Chem Res* **2015**, *48* (10), 2791-2802.
49. Stoumpos, C. C.; Mao, L. L.; Malliakas, C. D.; Kanatzidis, M. G., Structure-Band Gap Relationships in Hexagonal Polytypes and Low-Dimensional Structures of Hybrid Tin Iodide Perovskites. *Inorg Chem* **2017**, *56* (1), 56-73.
50. Wang, N. N.; Cheng, L.; Ge, R.; Zhang, S. T.; Miao, Y. F.; Zou, W.; Yi, C.; Sun, Y.; Cao, Y.; Yang, R.; Wei, Y. Q.; Guo, Q.; Ke, Y.; Yu, M. T.; Jin, Y. Z.; Liu, Y.; Ding, Q. Q.; Di, D. W.; Yang, L.; Xing, G. C.; Tian, H.; Jin, C. H.; Gao, F.; Friend, R. H.; Wang, J. P.; Huang, W., Perovskite light-emitting diodes based on solution-processed self-organized multiple quantum wells. *Nat Photonics* **2016**, *10* (11), 699-705.
51. Gao, L. L.; Li, X. T.; Traore, B.; Zhang, Y. L.; Fang, J.; Han, Y.; Even, J.; Katan, C.; Zhao, K.; Liu, S. Z.; Kanatzidis, M. G., m-Phenylenediammonium as a New Spacer for Dion-Jacobson Two-Dimensional Perovskites. *J Am Chem Soc* **2021**, *143* (31), 12063-12073.
52. Dhanabalan, B.; Castelli, A.; Palei, M.; Spirito, D.; Manna, L.; Krahne, R.; Arciniegas, M., Simple fabrication of layered halide perovskite platelets and enhanced photoluminescence from mechanically exfoliated flakes. *Nanoscale* **2019**, *11* (17), 8334-8342.
53. Ma, Z.; Li, F.; Sui, L.; Shi, Y.; Fu, R.; Yuan, K.; Xiao, G.; Zou, B., Tunable Color Temperatures and Emission Enhancement in 1D Halide Perovskites under High Pressure. *Advanced Optical Materials* **2020**, *8* (18), 2000713.
54. Smith, M. D.; Connor, B. A.; Karunadasa, H. I., Tuning the Luminescence of Layered Halide Perovskites. *Chem Rev* **2019**, *119* (5), 3104-3139.
55. Quarti, C.; Marchal, N.; Beljonne, D., Tuning the Optoelectronic Properties of Two-Dimensional Hybrid Perovskite Semiconductors with Alkyl Chain Spacers. *J Phys Chem Lett* **2018**, *9* (12), 3416-3424.
56. Bala, A.; Deb, A. K.; Kumar, V., Atomic and Electronic Structure of Two-Dimensional Inorganic Halide Perovskites  $A_{(n+1)}M_{(n)}X_{(3n+1)}$  ( $n=1-6$ ,  $A = \text{Cs}$ ,  $M = \text{Pb}$  and  $\text{Sn}$ , and  $X = \text{Cl}$ ,  $\text{Br}$ , and  $\text{I}$ ) from ab Initio Calculations. *J Phys Chem C* **2018**, *122* (13), 7464-7473.
57. Smith, M. D.; Jaffe, A.; Dohner, E. R.; Lindenberg, A. M.; Karunadasa, H. I., Structural origins of broadband emission from layered Pb-Br hybrid perovskites. *Chem Sci* **2017**, *8* (6), 4497-4504.
58. Cortecchia, D.; Yin, J.; Petrozza, A.; Soci, C., White light emission in low-dimensional perovskites. *Journal of Materials Chemistry C* **2019**, *7* (17), 4956-4969.
59. Febriansyah, B.; Borzda, T.; Cortecchia, D.; Neutzner, S.; Folpini, G.; Koh, T. M.; Li, Y.; Mathews, N.; Petrozza, A.; England, J., Metal Coordination Sphere Deformation Induced Highly Stokes-Shifted, Ultra Broadband Emission in 2D Hybrid Lead-Bromide Perovskites and Investigation of Its Origin. *Angew Chem Int Ed Engl* **2020**, *59* (27), 10791-10796.
60. Mao, L. L.; Kennard, R. M.; Traore, B.; Ke, W. J.; Katan, C.; Even, J.; Chabiny, M. L.; Stoumpos, C. C.; Kanatzidis, M. G., Seven-Layered 2D Hybrid Lead Iodide Perovskites. *Chem-US* **2019**, *5* (10), 2593-2604.
61. Mao, L. L.; Guo, P. J.; Kepenekian, M.; Spanopoulos, I.; He, Y. H.; Katan, C.; Even, J.; Schaller, R. D.; Seshadri, R.; Stoumpos, C. C.; Kanatzidis, M. G., Organic Cation Alloying on Intralayer A and Interlayer A' sites in 2D Hybrid Dion-Jacobson Lead Bromide Perovskites  $(A')(A)\text{Pb}_2\text{B}_7$ . *J Am Chem Soc* **2020**, *142* (18), 8342-8351.
62. Hadi, A.; Ryan, B. J.; Nelson, R. D.; Santra, K.; Lin, F. Y.; Cochran, E. W.; Panthani, M. G., Improving the Stability and Monodispersity of Layered Cesium Lead Iodide Perovskite Thin Films by Tuning Crystallization Dynamics. *Chem Mater* **2019**, *31* (14), 4990-4998.
63. Sidhik, S.; Li, W. B.; Samani, M. H. K.; Zhang, H.; Wang, Y. F.; Hoffman, J.; Fehr, A. K.; Wong, M. S.; Katan, C.; Even, J.; Marciel, A. B.; Kanatzidis, M. G.; Blancon, J. C.; Mohite, A. D., Memory Seeds Enable High Structural Phase Purity in 2D Perovskite Films for High-Efficiency Devices. *Adv Mater* **2021**, *33* (29), 2007176.
64. Reddy, G. N. M.; Malon, M.; Marsh, A.; Nishiyama, Y.; Brown, S. P., Fast Magic-Angle Spinning Three-Dimensional NMR Experiment for Simultaneously Probing H-H and N-H Proximities in Solids. *Anal Chem* **2016**, *88* (23), 11412-11419.